

# Growth of half-metallic $\text{CrO}_2$ nanostructures for superconducting spintronic applications

A. Singh<sup>1</sup>, C. Jansen<sup>1</sup>, K. Lahabi<sup>1</sup>, & J. Aarts<sup>1</sup>

<sup>1</sup>*Kamerlingh Onnes-Huygens Laboratory, Leiden University,  
P.O. Box 9504, 2300 RA Leiden, The Netherlands.*

(Dated: March 9, 2016)

Superconductor-ferromagnet (S-F) hybrids based on half-metallic ferromagnets, such as  $\text{CrO}_2$ , are excellent candidates for superconducting spintronic applications. This is primarily due to their fully spin polarized nature, which produces significantly enhanced long-range triplet proximity effects. However, reliable production of  $\text{CrO}_2$ -based Josephson junctions (JJs) is challenging, mainly because of the difficulty to control the transparency of the S/F interface. We have grown  $\text{CrO}_2$  nanowires by chemical vapor deposition on  $\text{TiO}_2$  substrates combined with selective area growth in trenches defined with amorphous  $\text{SiO}_x$ . This allows us to create lateral JJs, with the nanowire as the weak link. We show that the nature of the growth is highly anisotropic, and that the morphology of the  $\text{CrO}_2$  nanostructures changes systematically during the growth process, depending on the width of the trench. The detailed growth study enables us to synthesise multifaceted and highly homogeneous  $\text{CrO}_2$  wires. These are utilized to fabricate JJs with high S/F interface transparency, leading to large supercurrents. The well-defined geometry of the device allows us to reliably estimate an exceptionally high critical current density  $J_c = 10^9 \text{ Am}^{-2}$  over a distance of 600 nm.

Superconductor/Ferromagnet (S/F) hybrids have attracted great interest due their potential application in spintronic devices to minimize the dissipation/Joule heating, which is the biggest challenge for current-driven processes at the nanoscale [1–3]. The novelty of such hybrids lies in the generation of spin polarized triplet Cooper pairs in the ferromagnet [4–6]. They are generated by subjecting singlet Cooper pairs at the S/F interface to spin mixing and rotation [7], which is usually achieved by introducing another thin ferromagnetic layer at the interface [8–11]. Since triplet Cooper pairs are not affected by the exchange field of the ferromagnet, they can survive over considerably long distances, thereby giving rise to spin-polarized supercurrents. Fully spin polarized  $\text{CrO}_2$  is an ideal ferromagnet for such applications. The spatial extent of induced triplet correlations in  $\text{CrO}_2$  is of the order of a micron [12, 13], while it is limited to few tens of nm for standard ferromagnets (Co, Ni, Fe). Furthermore, the efficiency of the triplet generation is significantly enhanced, as demonstrated in recent experiments in a spin valve geometry [14, 15]. Though large supercurrents have been observed in  $\text{CrO}_2$  films [16], a serious bottleneck for further studies and applications of such Josephson junctions (JJs) has been the poorly controlled interface transparency, together with ill-defined current paths in the full film. Etching wire structures out of films proved no solution since the resist mask and the etch step are detrimental to the surface and bring extra disorder in the material. To address this issue, we have made a detailed investigation into the growth of  $\text{CrO}_2$  nanowires by selective area chemical vapor deposition (CVD).

A salient feature of the CVD growth of  $\text{CrO}_2$  is that it is only known to grow epitaxially on  $\text{TiO}_2$  or sapphire substrates. This is an advantage for selective area growth (SAG), whereby a patterned  $\text{SiO}_x$  mask can be used to

define the geometry of the  $\text{CrO}_2$  nanostructures. Previous reports on SAG of  $\text{CrO}_2$  focussed on the morphology of thick  $\text{CrO}_2$  structures but did not give insight into the nucleation and growth kinetics at the early stage of growth [17, 18]. Here, we demonstrate the effect of mask confinement, lattice mismatch anisotropy, and trench aspect ratio on the magnetic and structural morphology of  $\text{CrO}_2$  nanostructures at different stages of growth, covering a wide range of film thicknesses. A better understanding of SAG allows us to create high quality uniform  $\text{CrO}_2$  nanowires with well-defined facets resulting in transparent interfaces. In addition, we show that the magnetization state of the nanowire can be controlled by exploiting its shape anisotropy. This robust control over the magnetization and transparency enables us to reproducibly fabricate  $\text{CrO}_2$ -based JJs with large critical current densities. More generally, we have developed a device platform which will allow for a large variety of different wire, contact and magnetic domain geometries.

**Selective Area Growth** We start with a rutile (100)  $\text{TiO}_2$  substrate which has a tetragonal surface net ( $b = 0.459 \text{ nm}$ ,  $c = 0.296 \text{ nm}$ ), on which  $\text{CrO}_2$  ( $b = 0.442 \text{ nm}$ ,  $c = 0.292 \text{ nm}$ ) can be grown isostructurally. The lattice mismatch is anisotropic, being -1.4 % along the  $b$ -axis and -3.8 % along the  $c$ -axis, respectively. This leads to anisotropic growth rates, which is important for nanowire growth. Substrates were cleaned with organic solvents (Acetone/IPA) followed by HF treatment, on which a 25 nm  $\text{SiO}_x$  thin film was sputter-deposited. Using e-beam resist and lithography, openings of different sizes and shapes were created in the resist along different crystallographic directions.  $\text{SiO}_x$  was selectively removed from the openings using RIE etching with a  $\text{CF}_4$ - and an  $\text{O}_2$ -plasma. The etch time of  $\text{SiO}_x$  is critical because underetching results in only partial removal

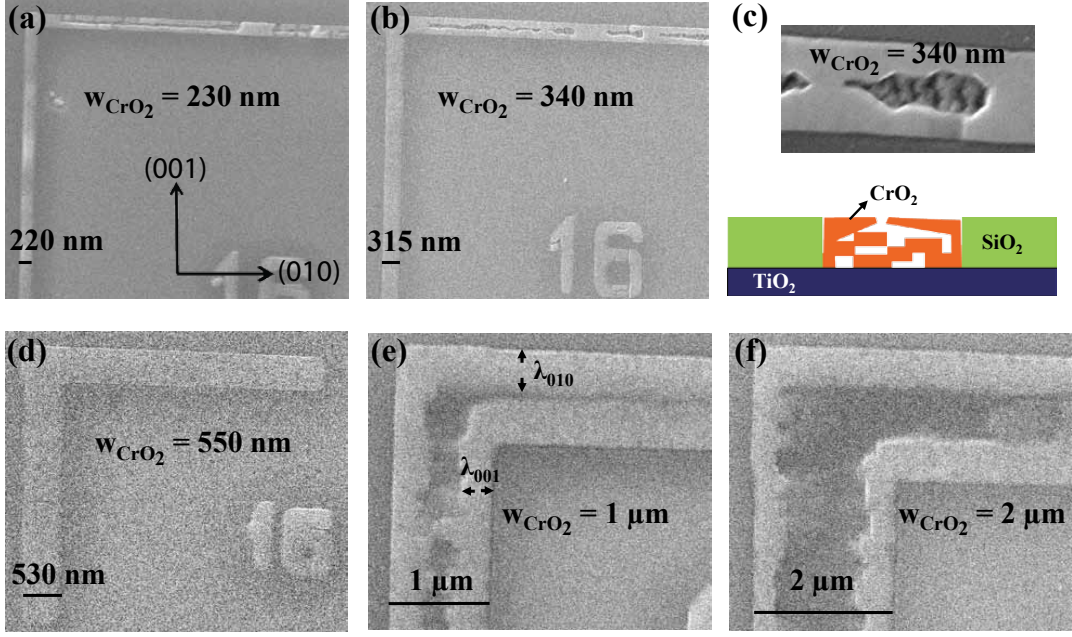


Figure 1: Scanning electron micrographs of L-shaped nanowires along the indicated directions, grown for 20 minutes, with trench widths (a) 230 nm, (b) 340 nm, (c) 340 nm, a close-up. The lower half schematically illustrates the growth mode for trench widths (d) 550 nm, (e) 1  $\mu\text{m}$ , and (f) 2  $\mu\text{m}$ . The measured width of the  $\text{CrO}_2$  bars is shown, and found equal to the trench width. In (d)  $\lambda$  is a measure for the surface diffusion length.

of  $\text{SiO}_x$  while overetching damages the underlying  $\text{TiO}_2$  substrate, which affects the film quality adversely. Next,  $\text{CrO}_2$  was grown selectively in the  $\text{SiO}_x$  trenches (trench depth 25 nm, trench width  $w_{\text{trench}}$ ) by CVD in a two-zone furnace where the substrate temperature was kept at 395°C while the precursor  $\text{CrO}_3$  was heated to 260°C in the presence of a flow of 100 sccm  $\text{O}_2$  carrier gas. By monitoring the growth times ( $t_g$ ), samples with varying thicknesses were prepared. Each sample consists of  $\text{CrO}_2$  structures with different sizes, shapes, aspect ratios and orientations. Scanning electron microscopy (SEM), Atomic force microscopy (AFM), and Magnetic force microscopy (MFM) were used to examine the structural and magnetic morphology of the  $\text{CrO}_2$  nanostructures.

**In-trench growth** Fig. 1a-e show the SEM images of L-shaped nanowires, grown for 20 minutes, with  $w_{\text{trench}}$  varying from 230 nm to 2  $\mu\text{m}$ . The time is chosen such that it fills the 25 nm deep trench. For the discussion, the width range is divided into two regimes, Regime I :  $w_{\text{trench}} \leq 2\lambda$ , and Regime II:  $w_{\text{trench}} \geq 2\lambda$ , where  $\lambda$  is a characteristic length bearing resemblance to a surface diffusion length, which is anisotropic due to the anisotropic lattice mismatch. For free films, growth results in the formation of rectangular  $\text{CrO}_2$  grains with their long axis along [001] and with an average size of  $\sim 300 \text{ nm} \times 100 \text{ nm}$ , which sets the scale for  $\lambda$ . In the strongly confined structures shown in Fig.1a-b, nucleation and growth is clearly anisotropic, with homogeneous wires forming along [001] and more inhomogeneous growth along [010]. This can

be understood from the better lattice match along [001] which also is the unconfined direction. Individual grains grow faster and coalesce to form a continuous and homogeneous wire. Along [010] the wires grow in a peculiar fashion, namely *from the sides* rather than from the bottom. Fig. 1c shows a close-up of the 340 nm trench where a smooth surface is seen at the sides, and a hole in the middle where, at the bottom, growth has also started. Apparently,  $\text{CrO}_2$  islands nucleate preferably at the  $\text{SiO}_x/\text{TiO}_2$  interface and grow laterally inward but also vertically upward. This dynamically inhibits the supply of the reactants towards the bottom of the trench, but it does allow inward lateral overgrowth starting higher up the wall. The result is a disordered structure with voids. This so-called nanopendepitaxy overgrowth (nPEO) is known from semiconductor growth, in particular for GaN, in the fabrication of nanoairbridges and suspended structures of GaN with superior quality [19–21].

At  $w_{\text{trench}} = 550 \text{ nm}$  (Fig.1d) Regime II starts and the growth changes to a homogeneous filling of the trench [22]. Islands nucleate along the walls and "quantum fortress"-like structures are formed irrespective of the orientation of trenches [23]. Increasing  $w_{\text{trench}}$  to 1  $\mu\text{m}$  and 2  $\mu\text{m}$  (Fig.1e,f) the filling becomes inhomogeneous again, with the middle of the trench empty but now because the growth fronts propagating from the walls do not reach the middle. We assume that the size of the  $\text{CrO}_2$  strip along the walls is determined by  $\lambda$  and we

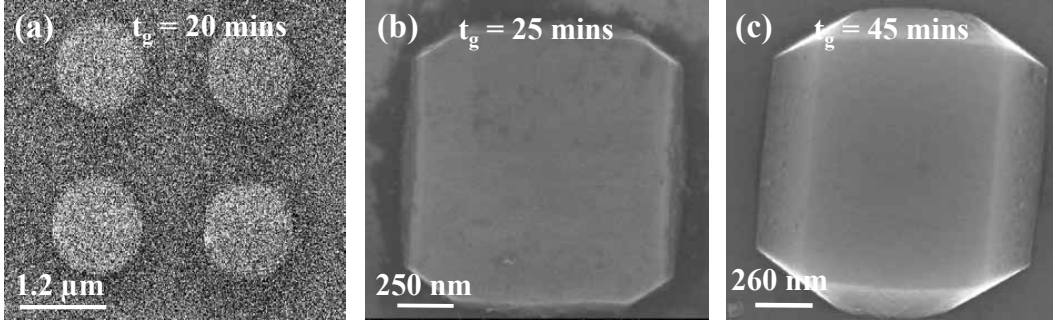


Figure 2: Scanning electron micrographs of  $\text{CrO}_2$  structures, grown in circular  $\text{SiO}_2$  trenches, for (a) 20 minutes (filling the disk-shaped trench), (b) 25 minutes, and (c) 45 minutes. The latter two are overgrowth structures.

observe  $\lambda_{010} \sim 450$  nm and  $\lambda_{010} \sim 300$  nm independent of  $w_{\text{trench}}$ . Note that these results are quite different from earlier reports on SAG of  $\text{CrO}_2$ , where it was assumed that  $\text{CrO}_2$  nucleates and grows uniformly in the narrow trenches away from the  $\text{SiO}_x$  side walls [18]. Our results present a very different picture, with important new aspects for  $\text{CrO}_2$  nanowire growth.

**Lateral overgrowth** Next we focus on the lateral epitaxial overgrowth (LEO) above the  $\text{SiO}_x$  mask at higher  $t_g$ . Fig. 2a-c shows the evolution of the structural morphology of  $\text{CrO}_2$ , grown in circular trenches, for different  $t_g$ . For  $t_g = 20$  minutes, no overgrowth yet occurs, resulting in the formation of  $\text{CrO}_2$  discs. With further increase in  $t_g$  (25 minutes),  $\text{CrO}_2$  starts to overgrow laterally on  $\text{SiO}_x$ . Important to realize is that there is no epitaxial relation with the amorphous  $\text{SiO}_x$ , so this is sideways growth starting from the structure coming out of the trench. The development of (011) facets can be observed, assumedly to minimize the total surface energy, although the facets formed at this stage are rough with step edges. For  $t_g = 45$  minutes, the  $\text{CrO}_2$  islands exhibit fully developed facets with smooth surfaces. This type of facet evolution with growth time has been reported recently for SAG of GaN [22].

In order to isolate the effect of lattice mismatch and size on the issue of  $\text{CrO}_2$  overgrowth, we also prepared rectangular 500 nm wide  $\text{SiO}_x$  trenches oriented between the (010)- ( $\theta = 0^\circ$ ) and (001)-directions ( $\theta = 90^\circ$ ), at intervals of  $15^\circ$ . The structural morphologies were characterized at different stages (thicknesses) of growth. In Fig. 3a schematic of the LEO is outlined and Fig 3b,c show the SEM images of  $\text{CrO}_2$  nanowires, with  $t_g = 20$  minutes, and 45 minutes, respectively. Clearly, there is no anisotropy in the lateral growth for in the first 20 minutes of growth while it is highly anisotropic for  $t_g = 45$  minutes. As shown in Fig. 3c, the nanowires exhibit jagged facets at the intermediate angles which is attributed to the higher growth rate along (001) [17]. The anisotropy of lateral overgrowth with SAG has been reported earlier for thick  $\text{CrO}_2$  structures [17, 18]. However,

from our data we can extract additional and quantitative information on the anisotropy in lateral as well as vertical overgrowth over a range of sizes and thicknesses. In Fig. 3d we plot the full width of the nanowire as measured from Fig. 3c. This exhibits a maximum at  $\theta = 60^\circ$  and becomes more pronounced with increasing  $t_g$ . The direction coincides with the diagonal of the  $\text{CrO}_2$  unit cell. In Fig. 3e we plot the lateral overgrowth (defined as the difference between the total width of the  $\text{CrO}_2$  nanowire and the trench width) as function of  $\theta$  for different trench widths up to 500 nm (Regime I). The Figure shows that the lateral overgrowth hardly depends on trench width for the various angles, confirming that it is mainly determined by the thickness and anisotropic strain. Finally, to study the anisotropy in vertical growth, AFM was used to determine the thickness of the nanowires grown for different times up to  $t_g = 45$  minutes. Fig. 3f again shows suggests that during the first 20 minutes the  $\text{CrO}_2$  growth front just reaches the top of the  $\text{SiO}_2$  trench and the thickness is isotropic. For higher growth times the vertical overgrowth becomes anisotropic, now with the minimum along  $\theta = 60^\circ$ : lateral overgrowth clearly goes at the expense of vertical overgrowth, with the largest effect around  $60^\circ$  from the (010)-direction. This is in contrasts with the previous reports on SAG of  $\text{CrO}_2$  structures where vertical overgrowth was reported to be isotropic [17].

More formally, the correlation between the vertical and the lateral overgrowth, can be understood from the mass transport mechanism i.e. absorption or desorption of adatoms on different facets of  $\text{CrO}_2$  during the CVD growth. The vertical growth depends on the impinging flux on top and on the sides of the growing surface and also on the diffusion flux from the substrate to the top surface [24]. The size dependence of the vertical growth rate is given by the following expression,

$$dH/dt = \gamma_{\text{top}} + \gamma_{\text{sw}}/D + \gamma_{\text{sub}}/D^2, \quad (1)$$

where  $H$  is the height,  $D$  is the width of the structures,  $\gamma_{\text{top}}$ ,  $\gamma_{\text{sw}}$ , and  $\gamma_{\text{sub}}$  are the constants related to surface

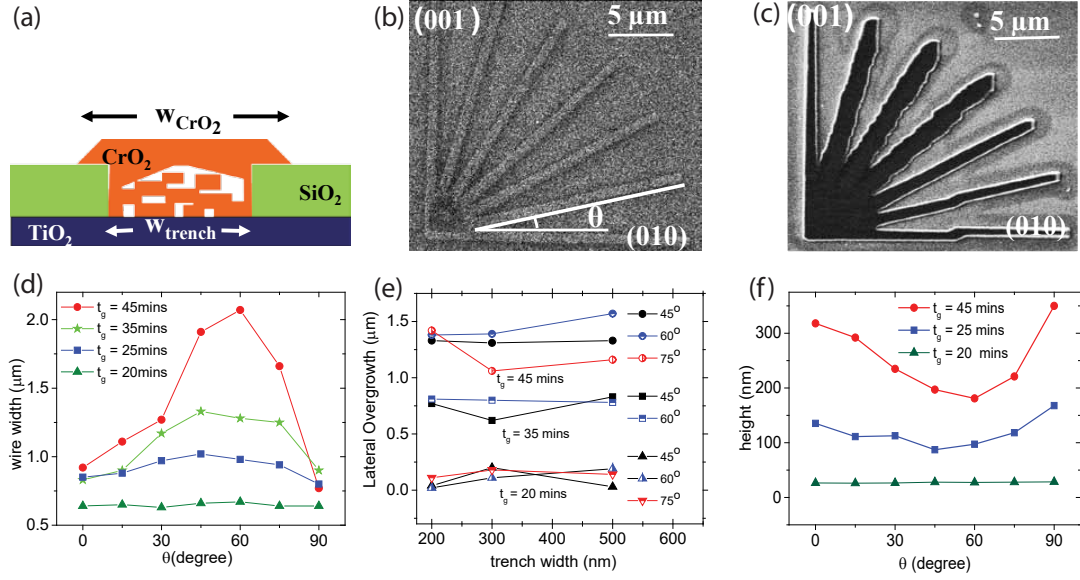


Figure 3: (a) Schematic of lateral epitaxial overgrowth of CrO<sub>2</sub> over SiO<sub>2</sub> for higher growth times. Scanning electron micrographs of CrO<sub>2</sub> nanowires oriented between  $\theta = 0^\circ$  and  $\theta = 90^\circ$  at the intervals of  $15^\circ$  and grown in 500 nm wide trenches for (b) 20 minutes, and (c) 45 minutes. (d) Angular dependence of width of CrO<sub>2</sub> nanowires ( $w_{CrO_2}$ ). (e) lateral over growth ( $w_{CrO_2} - w_{trench}$ ) as a function of trench width ( $w_{trench}$ ) along  $\theta = 45^\circ, 60^\circ$ , and  $75^\circ$  for different growth times. (f) Angular dependence of height of CrO<sub>2</sub> nanowires, grown in 500 nm wide SiO<sub>x</sub> trenches, for different times.

impingement on top and side wall and diffusion from the substrate, respectively. In this simple picture, the maximum lateral overgrowth corresponds to largest  $D$  and hence lowest vertical overgrowth. Furthermore, with change in orientation of the wire,  $\gamma_{top}$  remains constant while the contribution from  $\gamma_{sw}$ , and  $\gamma_{sub}$  decreases due to the formation of jagged edges at the intermediate angles. Nonuniform / ragged edges prevent the surface diffusion of adatom on the side walls and also from the substrates, slowing down the vertical overgrowth.

**Magnetic domains** Next we discuss the magnetic domain structures of our nanowires. Domain behavior has been studied both in early SAG investigations [18] and in etched wires [25, 26] and it is well known that for CrO<sub>2</sub> films on TiO<sub>2</sub> the [001] direction is the magnetic easy axis while the [010] direction is the magnetic hard axis, as a consequence of the strain. Fig.4a shows the magnetic structure of wires of different size along different crystallographic orientations as measured by using magnetic force microscopy (MFM). The wires oriented along [001] are in a single domain state, as seen from the absence of any contrast in MFM image, and in the cross-section shown in the lowest panel of Fig. 4b. When the wire is rotated away from the easy axis, striplike domains start appearing in the wires to minimize the total magnetic energy. This can be seen by dark/bright contrast the MFM micrograph (Fig. 4a) and as oscillations in the magnetic contrast (top and middle panel Fig. 5b). We observe that the domain size is also direction dependent with a minimum along the [001] axis, which is the hard axis. The

wires therefore behave as expected.

**Supercurrents** As mentioned in the introduction, fully spin-polarized ferromagnetic nanowires are of interest for superspintronics applications, and here we show that we can fabricate Josephson junctions with the CrO<sub>2</sub> nanowire as weak link. First we grow a nanowire along the easy axis [001] in order to have the magnetization along the wire axis. Next we use lift-off and sputtering to deposit rectangularly shaped contacts of (Cu or Ag)(5 nm)/Ni(1.5 nm)/MoGe(125 nm) trilayer stacks, with their long axis perpendicular to CrO<sub>2</sub> wire, i.e. along the [010] direction as shown in Fig. 5a. The distance between the contacts is typically 500 nm. The shape anisotropy aligns the magnetization of the Ni layer in the contact stack along the crystal [010] direction, which is very effective in providing maximum non-collinearity at the interface, a key ingredient for triplet generation. In the trilayer stack we used either Cu or Ag to prevent exchange coupling between the CrO<sub>2</sub> and Ni layers. Amorphous MoGe is the superconductor used to induce the proximity effect. Since at the surface CrO<sub>2</sub> inevitably reduces to the antiferromagnetic insulator Cr<sub>2</sub>O<sub>3</sub> we clean it in-situ with a brief Ar-etch prior to the trilayer contact deposition. In this report, we present the results obtained on two JJ devices, one with Cu and one with Ag as spacer layer, named J1 and J2, respectively. The other parameters of J1 and J2 are provided in the table below.

Fig.5b shows a plot of resistance  $R$  versus temperature ( $T$ ) for J1 measured in a quasi-4-point geometry, meaning

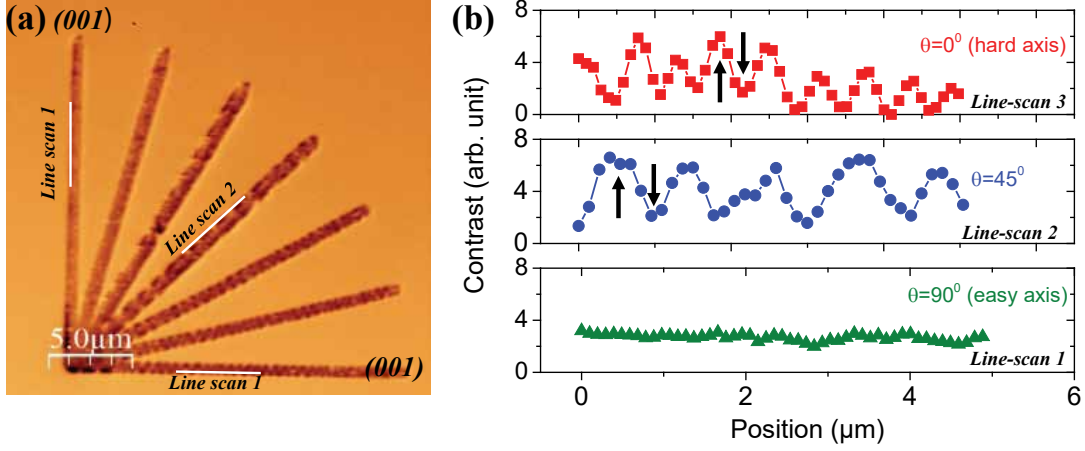


Figure 4: (a) Magnetic force micrograph of  $\text{CrO}_2$  nanowires grown in 500 nm wide trench, oriented between  $\theta = 0^\circ$  and  $\theta = 90^\circ$  at the intervals of  $15^\circ$ . White along the edges of the wires represent the line scan used to determine the phase magnetic phase contrast. (b) Magnetic phase contrast along the edges of the wires for  $\theta = 0^\circ$  (upper panel),  $\theta = 45^\circ$  (middle panel), and  $\theta = 90^\circ$  (lower panel). up and down arrow represent the opposite orientation ( $180^\circ$ ) domains

Table I: parameters of two Josephson Junction devices based on  $\text{CrO}_2$  nanowires. The values for  $R_N$  were calculated using a specific resistivity of  $6 \mu\Omega\text{cm}$ .

Device	width	thickness	junction length	$R_N$
J1 (Cu)	$1 \mu$	75 nm	400 nm	0.32 Ohm
J2 (Ag)	500 nm	150 nm	600 nm	0.48 Ohm

that the interface resistance is part of the total normal state resistance.  $R$  disappears around 6.5 K, but there is a finite resistance tail down to 5 K, where  $R$  reaches 0 (c.q. the measurement limit). Below 5 K, supercurrents can be measured. Fig. 5c shows the current-voltage (I-V) characteristics of J1 at different temperatures from which the critical current of the weak link (the proximized  $\text{CrO}_2$ ) can be determined. Interestingly, despite its lower junction length (see Table I), J1 has a lower critical current density than J2, which is probably due to lower interface transparency. Our earlier studies did not use Ag, but the result indicates that the use of Cu might lead to degradation of the interface by the formation of some oxide. Fig. 5d displays the variation of critical current density as a function temperature for J1 and J2, and as expected,  $I_c$  increases monotonically with the decrease in temperature. The measured resistance of the device is dominated by the Cu layer in the leads, since the Cu specific resistivity  $\rho_{0,\text{Cu}}$  of the order of  $5 \mu\Omega\text{cm}$  is much smaller than  $\rho_{0,\text{MoGe}} \approx 200 \mu\Omega\text{cm}$ . Taking a length of 70  $\mu\text{m}$  per lead, a width of 2.5  $\mu\text{m}$  and a thickness of 5 nm, we find 560  $\Omega$ . The normal resistance of the  $\text{CrO}_2$  weak link we estimate using  $\rho_{0,\text{CrO}_2} \approx 6 \mu\Omega\text{cm}$  (the thin films value for the easy axis) to be 0.32  $\Omega$ . This leaves about 20  $\Omega$  as the contact resistance. We note in Fig. 5b that the low-temperature  $R$  is well below 0.32  $\Omega$ , and in Fig. 5c

that the voltage increase above  $I_c$  starts with a small steep slope, but then settles to a slope which is close to 0.3  $\Omega$ , quite as expected for the  $\text{CrO}_2$  weak link. Analyzing the junction behavior a bit further, in the long junction limit  $I_c$  is proportional to  $T^{3/2} \exp(2\pi k_B T / E_{th})^{-1/2}$  where  $E_{th} = \hbar D / L^2$  is the Thouless energy of the junction with diffusion coefficient  $D$  and junction length  $L$ . Therefore, the slope of the plot of  $\ln(I_c) - 3/2 \ln(T)$  vs  $T^{1/2}$ , shown in the inset, can be used to estimate the Thouless energy  $E_{Th}$  which is 11  $\mu\text{V}$ . From this number we can estimate  $D$  to be  $2.7 \times 10^{-3} \text{ m}^2/\text{s}$ , which is close to numbers obtained before. Using a Fermi velocity of  $2.2 \times 10^5 \text{ m/s}$  [27] it corresponds to a mean free path of 36 nm which suggests that our JJS are in long (diffusive) junction limit.

**Conclusions** To conclude, we have made a detailed study of growth kinetics of halfmetallic ferromagnetic  $\text{CrO}_2$  nanowires by selective area growth on  $\text{TiO}_2$ , in 25 nm deep trenches defined by a  $\text{SiO}_x$  mask. At an early stage of growth ( $t_g = 20$  minutes), for trench width below 500 nm we find that thin homogeneous wires can be grown along [001], while along [010] the growth is highly disordered, with voids, formed in a fashion called nanopendepo epitaxy. Above a trench width of 500 nm, the trench is lined by  $\text{CrO}_2$  strips formed along the edges with nonuniformity at the center. By increasing the growth time, uniform  $\text{CrO}_2$  structures are formed due to the lateral overgrowth over  $\text{SiO}_x$  mask. Wires grown along the magnetic easy axis, which is the [001] direction, were contacted with stacks of Cu/Ni/MoGe and Ag/Ni/MoGe, which allowed us to study triplet supercurrents. This upholds the earlier observation of very high supercurrent densities of order  $10^9 \text{ A/m}^2$  at 4.2 K over a distance of 600 nm.  $\text{CrO}_2$  wire based Josephson junctions will make it now possible to characterize the in-



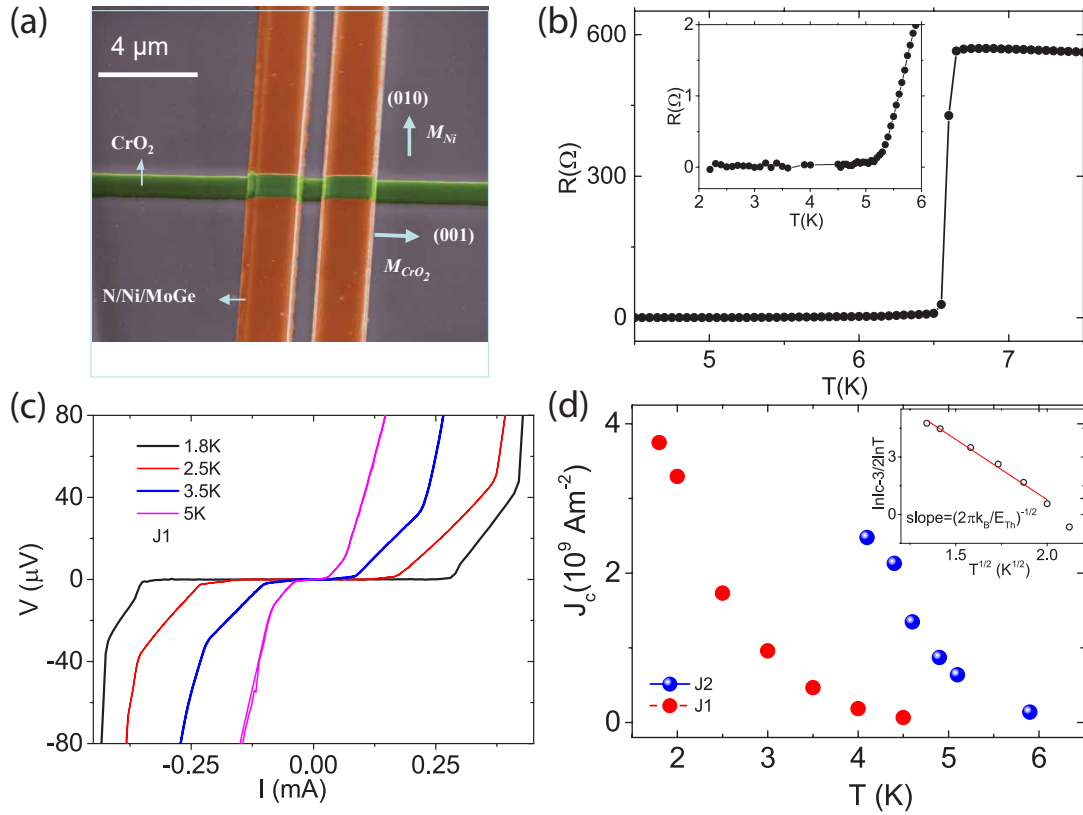


Figure 5: (a). Scanning electron micrograph (false color) of a Josephson Junction on a CrO<sub>2</sub> nanowire (green). The graph also shows crystal and magnetization directions. Orange contacts pads consist of trilayer (Cu or Ag)/Ni/MoGe. (b) Resistance  $R$  versus temperature  $T$  for junction J1. The inset shows the behavior around zero resistance (c) Current  $I$  versus voltage  $V$  characteristics of J1 at different temperatures. (d) Critical current density  $J_c$  versus  $T$ ; the inset shows a linear fit to a plot of  $\ln(I_c) - 3/2 \ln(T)$  vs  $T^{1/2}$ .

interfaces fully, make reliable measurements of the dependence of critical current on junction length, and study the influence of magnetic domains in the supercurrent path.

**ACKNOWLEDGEMENTS** Technical support from M.B.S. Hesselberth, D. Boltje, and A. F. Beker are gratefully acknowledged. This work is part of the research programme of the Foundation for Fundamental Research on Matter (FOM), which is part of the Netherlands Organisation for Scientific Research (NWO). The work was also supported by the EU COST action MP1201 'NanoSC' and by a grant from the Leiden-Delft Consortium 'NanoFront'.

- [1] Matthias Eschrig. Spin-polarized supercurrents for spintronics: a review of current progress. *Reports on Progress in Physics*, 78(10):104501, 2015.
- [2] J. Linder and J. W. A. Robinson. Superconducting spintronics. *Nature Physics*, 11:307, 2015.
- [3] N. G. Pugach and A. I. Buzdin. *Applied Physics Letters*, 2012.
- [4] FS Bergeret, AF Volkov, and KB Efetov. Long-range proximity effects in superconductor-ferromagnet structures. *PHYSICAL REVIEW LETTERS*, 86(18):4096–4099, APR 30 2001.
- [5] M. Eschrig, J. Kopu, J. C. Cuevas, and Gerd Schön. Theory of half-metal/superconductor heterostructures. *Phys. Rev. Lett.*, 90:137003, Apr 2003.
- [6] M. Houzet and A. I. Buzdin. Long range triplet Josephson effect through a ferromagnetic trilayer. *PHYSICAL REVIEW B*, 76(6), AUG 2007.
- [7] M. Eschrig and T. Lofwander. Triplet supercurrents in clean and disordered half-metallic ferromagnets. *Nat*

- Phys*, 4:138, 2008.
- [8] Trupti S. Khaire, Mazin A. Khasawneh, W. P. Pratt, Jr., and Norman O. Birge. Observation of Spin-Triplet Superconductivity in Co-Based Josephson Junctions. *PHYSICAL REVIEW LETTERS*, 104(13), APR 2 2010.
  - [9] E. C. Gingrich, P. Quarterman, Yixing Wang, R. Loloee, W. P. Pratt, Jr., and Norman O. Birge. Spin-triplet supercurrent in Co/Ni multilayer Josephson junctions with perpendicular anisotropy. *PHYSICAL REVIEW B*, 86(22), DEC 12 2012.
  - [10] J. W. A. Robinson, J. D. S. Witt, and M. G. Blamire. Controlled injection of spin-triplet supercurrents into a strong ferromagnet. *Science*, 329(5987):59–61, 2010.
  - [11] N. Banerjee, J.W.A. Robinson, and M. G. Blamire. Reversible control of spin-polarized supercurrents in ferromagnetic josephson junctions. *Nat Commun*, 5:4771, 2014.
  - [12] RS Keizer, STB Goennenwein, TM Klapwijk, GX Miao, G Xiao, and A Gupta. A spin triplet supercurrent through the half-metallic ferromagnet CrO<sub>2</sub>. *NATURE*, 439(7078):825–827, FEB 16 2006.
  - [13] M. S. Anwar, F. Czeschka, M. Hesselberth, M. Porcu, and J. Aarts. Long-range supercurrents through half-metallic ferromagnetic CrO<sub>2</sub>. *PHYSICAL REVIEW B*, 82(10), SEP 3 2010.
  - [14] A. Singh, S. Voltan, K. Lahabi, and J. Aarts. Colossal proximity effect in a superconducting triplet spin valve based on the half-metallic ferromagnet cro<sub>2</sub>. *Phys. Rev. X*, 5:021019, May 2015.
  - [15] X. L. Wang, A. Di Bernardo, N. Banerjee, A. Wells, F. S. Bergeret, M. G. Blamire, and J. W. A. Robinson. Giant triplet proximity effect in superconducting pseudo spin valves with engineered anisotropy. *PHYSICAL REVIEW B*, 89(14), APR 30 2014.
  - [16] M. S. Anwar, M. Veldhorst, A. Brinkman, and J. Aarts. Long range supercurrents in ferromagnetic CrO<sub>2</sub> using a multilayer contact structure. *Appl. Phys. Lett.*, 100(5), JAN 30 2012.
  - [17] A. Gupta, X. W. Li, S. Guha, and Gang Xiao. Selective-area and lateral overgrowth of chromium dioxide (cro<sub>2</sub>) films by chemical vapor deposition. *Applied Physics Letters*, 75(19), 1999.
  - [18] Xiaojing Zou and Gang Xiao. Magnetic domain configurations of epitaxial chromium dioxide (cro<sub>2</sub>) nanostructures. *Applied Physics Letters*, 91(11), 2007.
  - [19] Isaac H. Wildeson, David A. Ewoldt, Robert Colby, Eric A. Stach, and Timothy D. Sands. Controlled growth of ordered nanopore arrays in gan. *Nano Letters*, 11(2):535–540, 2011. PMID: 21171632.
  - [20] Y. D. Wang, K. Y. Zang, S. J. Chua, S. Tripathy, P. Chen, and C. G. Fonstad. Nanoair-bridged lateral overgrowth of gan on ordered nanoporous gan template. *Applied Physics Letters*, 87(25), 2005.
  - [21] Zheleva T. S., Smith A. S., Thomson D. B., Linthicum K. J., Rajagopal P., and Davis R. F. . Pendeo-epitaxy: A new approach for lateral growth of gallium nitride films. *Journal of Electronic Materials*, 28(4), 1999.
  - [22] A. et al. Tanaka. Strong geometrical effects in submillimeter selective area growth and light extraction of gan light emitting diodes on sapphire. *Sci. Rep.*, 5(19), 1999.
  - [23] Thomas E. Vandervelde, Piyush Kumar, Takeshi Kobayashi, Jennifer L. Gray, Tim Pernel, Jerrold A. Floro, Robert Hull, and John C. Bean. Growth of quantum fortress structures in silxgex/si via combinatorial deposition. *Applied Physics Letters*, 83(25):5205–5207, 2003.
  - [24] Xue Wang, Jana Hartmann, Martin Mandl, Matin Sadat Mohajerani, Hergo-H. Wehmann, Martin Strassburg, and Andreas Waag. Growth kinetics and mass transport mechanisms of gan columns by selective area metal organic vapor phase epitaxy. *Journal of Applied Physics*, 115(16), 2014.
  - [25] C. König, M. Fonin, M. Laufenberg, A. Biehler, W. Bührer, M. Kläui, U. Rüdiger, and G. Güntherodt. Micromagnetism and magnetotransport properties of micron-sized epitaxial cro<sub>2</sub> (100) wires. 75:144428, Apr 2007.
  - [26] A. Biehler, M. Kläui, M. Fonin, C. König, G. Güntherodt, and U. Rüdiger. Micromagnetism and magnetotransport properties of micron-sized epitaxial cro<sub>2</sub> (100) wires. 75:184427, Apr 2007.
  - [27] S. P. Lewis, P. B. Allan, and T. Sasaki. Band structure and transport properties of cro<sub>2</sub>. 55:10253, 1997.